

# GAD-Generative Learning for HD Map-Free Autonomous Driving

Weijian Sun, Yanbo Jia, Qi Zeng, Zihao Liu, Jiang Liao, Yue Li, Xianfeng Li, Bolin Zhao  
JIDU AUTO

## Abstract

*Deep-learning-based techniques have been widely adopted for autonomous driving software stacks for mass production in recent years, focusing primarily on perception modules, with some work extending this method to prediction modules. However, the downstream planning and control modules are still designed with hefty handcrafted rules, dominated by optimization-based methods such as quadratic programming or model predictive control. This results in a performance bottleneck for autonomous driving systems in that corner cases simply cannot be solved by enumerating hand-crafted rules. We present a deep-learning-based approach that brings prediction, decision, and planning modules together with the attempt to overcome the rule-based methods' deficiency in real-world applications of autonomous driving, especially for urban scenes. The DNN model we proposed is solely trained with 10 hours of human driver data, and it supports all mass-production ADAS features available on the market to date. This method is deployed onto a Jiyue test car with no modification to its factory-ready sensor set and compute platform. The feasibility, usability, and commercial potential are demonstrated in this article.*

## 1. Introduction

Autonomous driving software on the market to date usually is designed following a classical engineering methodology called “divide and conquer”, where the problem is divided into smaller sub-tasks to reduce complexity. These sub-tasks usually include perception, prediction, motion planning, and control. However, this easily interpretable rule-based method is highly dependent on accurate prior knowledge, which severely restricts its scalability. High-definition (HD) maps, among various forms of prior knowledge, play a crucial part in offering rich semantic information, including topology at both lane and road levels, lane geometries, crosswalks, traffic lights, intersections, etc. This prior information, with superior accuracy, greatly lessens the burden of perception and enormously facilitates planning tasks for autonomous driving. Unfortunately, HD

maps are proven hard to scale up due to the complexity and costliness of map generation and maintenance, as well as failure to reflect changes in real-world road conditions timely, which is often constrained by resource-intensive collection processes. For instance, lane reduction or expansion, changes in merge or diverge points, and lane closure or lane shifts due to roadblocks, barricades, and temporary construction zones are often seen in reality promptly but reflected on HD maps with months' of delay.

Furthermore, the rule-based planning module is held accountable for most failures and deficiencies of the autonomous driving system in real driving scenarios, especially for urban scenes, hence it is often regarded as the bottleneck of the entire software stack. New rules must be designed and re-tuned in accordance with different driving scenarios and new corner cases. This process is expensive and it scales poorly for the simple fact that the scenario space for the SDV is infinite while rules can only be of limited number.

End-to-end autonomous driving aims to consider sub-tasks in a full-stack manner jointly have been proposed to resolve the above issues. Methods [3, 7, 20–22, 24, 25, 38, 40, 48, 49] that direct learning from raw sensor data to planning trajectories or driving commands eliminate the need for manual planning rules and prerequisite HD maps, leading to efficient data utilization and adaptability to diverse driving scenarios. However, those works lack interpretability since omitting modularized results and are difficult to optimize. Interpretability is of key importance in a safety-critical system, particularly if a bad event were to happen in mass production. Moreover, the absence of modularized structure and prior knowledge makes these methods very brittle when deployed in real-world closed-loop.

To overcome the aforementioned problems, we explore an alternative method which runs entirely on the edge and purely relied on on-the-fly computation of local topology reconstructed with landmarks and occupancy grids [12] based on perception results. The reconstruction is designed to support motion planning in urban scenarios, and we explore its practicality for daily commuting first. We believe this is effective for two primary reasons. Firstly, landmarks (lane center, lane divider, road boundary, and pedes-

trian crossing) provide sufficient cues for driving in a cruise scenario - it generally consists of lane keep and lane change for following and overtaking behaviors regardless of how road topologies are organized. Second, for turning scenes (left turn, right turn, u-turn), we gather routing information from SD map or historical commuting trajectory and avoid collisions with the help of real-time occupancy.

To break the bottleneck brought by rule-based planning but maintain the system’s explainability and stability, we take modularized outputs from perception and propose a general framework to handle the prediction-planning tasks in a data-driven and integrated manner. Our framework consists of a trajectory generator and evaluator. The generator utilizes vectorized embedding from parametric input to perform trajectory generation, while the evaluator leverages rasterized non-parametric info in grid form to validate and score candidates with physically feasible output that can navigate in HD map-free. We validate our framework in a closed loop by deploying and testing it in real-world user-level autonomous driving vehicles.

We illustrate the pros of our design that decouple perception from the end-to-end stack: Firstly, the decoupled tasks are both constructed in an end-to-end way, benefiting from efficient data utilization but maintaining system’s stability and robustness. Secondly, the prediction-planning integration omits the parameterized prediction output, modeled in prior Gaussian distribution, which cannot always hold, thus avoiding information loss for downstream planning. The perception task is deterministic based, as long as the measurement is sufficient, therefore, less affected. Thirdly, the original tools for perception and planning can be reused for these two tasks. Otherwise, prerequisites of 3d construction at the sensor level like Nerf [14] are heavily resource-consuming.

The real-world closed-loop validation needs to be highlighted as well for the following reasons: Firstly, a closed-loop planner will adjust to the target in the loop to keep safe and comfortable since real-world planning needs to take into account the deviations brought by the controller’s modeling errors and external disturbances, which are omitted and thus cannot be tested by the open-loop planner. Secondly, the validity of the trajectory cannot be verified from the perspective of the downstream controller. The open-loop tests end when the trajectories are generated and compared with the recorded ones. However, unexpected and unreasonable jerks and curvatures, which can only be tested when the controller is in the loop, are usually ignored, and thus, the results become less convincing. This leaves the effectiveness of those methods (like UniAD [22], VAD [24], mile [20], ST-P3 [21]) unknown for onboard road tests and mass production.

Our key contributions are summarized as follows:

1. We propose an industry-level paradigm for data-driven

prediction-planning with an HD map-free setting. Our model leverages non-parametric information with better tolerance to upstream perception and handling prediction and planning tasks in one backbone.

2. To the best of our knowledge, we are the first evaluation of such system in a complex, real-world, urban road with a factory-ready sensor set and compute platform. We demonstrate the imperative of closed-loop evaluation compared to imitation metric adopted by extensive offline studies.
3. We extend the state-of-the-art data-driven approach and propose a method that goes beyond simple imitation or trajectory sampling and instead reasons about the potential in generative learning by combining max margin planning with multi-modal imitation.

## 2. Related work

### 2.1. End to End Learning

End-to-end autonomous driving and its effectiveness have been investigated recently. There exists a body of research [20, 24, 40, 47] focused on closed-loop end-to-end driving within simulators [10, 27]. However, a domain gap persists between the simulator environment and the real world, particularly concerning sensor data and the motion status of agents. Recently, open-loop end-to-end autonomous driving has attracted more attention. End-to-end autonomous driving methods [22, 24] that involve learning intermediate tasks claim their effectiveness in improving final planning performance. Nevertheless, the effectiveness of open-loop demonstration has been challenged recently [28], in terms of imbalanced data distribution and metric limitation. We tackle and bypass that controversial issue by validating our method in a real-world closed-loop road test.

Our work combines actor perception and scene occupancy as inputs for our paradigm. First, we demonstrate how off-the-shelf planners can use parametric results to enhance the quality of trajectory generation. Second, we show how to evaluate the generated trajectory with scene information as additional supervision. Third, we demonstrate the feasibility of combining scene-level occupancy and parametric landmarks as a replacement for an HD map in an urban area.

### 2.2. Data Driven Prediction

For actor-based trajectory predictions, these methods either generate a fixed set of trajectories [2, 4, 32, 50], or draw samples via generative modeling to characterize the distribution [17, 26, 36, 41]. In order to encode scene context, a classic CNN architecture can be applied to a rasterized map to predict 2D coordinates [8]. More recently, methods have started to leverage the graph obtained from HD-

map in order to better represent lane connectivity. VectorNet [13] encodes map and agent as polylines with a global interaction graph. LaneGCN [29] treats actor past and the lane graph separately and then fuses them with a series of attention layers. Temporal occupancy maps [19, 23, 37], on the other hand, provide another option to forecast grid or heat map at the scene level. We follow the philosophy of [11, 18, 38, 42, 46] in modeling scene-level representations, but propose a multi-stage pipeline to perform forecasting in both formats. Moreover, unlike typical methods, which heavily rely on the precision of trajectory output, our agent results are mainly adopted in the safety layer and to boost some of our samplers.

### 2.3. Data Driven Planning

For implicit planning methods, the network directly generates planned trajectory or control commands with direct and simple design [1, 5, 20, 25, 30, 33]. But it suffers from robustness and lack of interpretability [6]. For trajectory-based methods, modeling strategies from trajectory prediction are adopted, which build an imitation decoder trained under the supervision of human demonstration. PlanT [35] proposed a transformer-based backbone in actor-level representation and validated in simulation. SafetyNet [44] developed an ML planner and tested it in downtown San Francisco, but it relies on a fallback layer to handle algorithm failure with a traditional rule-based system. VAD [24] models the driving scene as a fully vectorized representation. More recently, explicit methods have been shown to adapt better to more challenging environments. Such approaches usually build a cost map with a trajectory sampler to generate the desired trajectory by choosing the optimal candidate with the lowest cost. The cost map is organized in a non-parametric form learned directly from the network [3, 7, 38, 48, 49]. Start with the pioneering work on NMP [48], extended by DSDNet [49] and P3 [38] that combined hand-crafted and learning-based costs to obtain an integrated cost volume. In the follow up works, MP3 [3] introduced mapless, while STP3 [21] explored vision-based inputs. We also adopt this combination to choose the best trajectory but extend the system’s robustness by boosting the generating algorithm with modularized perception output. In contrast to all the above methods, which solely rely on a rule-based sampler, our paradigm leverages imitation learning to build a diversified hybrid trajectory set and stays safe by being evaluated in an interpretable cost volume as a summary of scene occupancy and agent motion.

## 3. Methods

### 3.1. Input Representation

We make the assumption that we have access to a black-box perception module which can effectively map low-level

sensor data to 3D-tracked entities, visible landmarks, and scene occupancy. At each timestamp, we are provided with measured states for each tracked entity, including their 2D positions, velocities, and accelerations. Furthermore, the perception module also supplies information on all visible landmarks and road boundaries in front of our ego. Stop lines are also provided when they become visible as the SDV approaches the junction area. The above obstacles and landmarks are either described by coordinates or measured by polynomial curves, referred to as the parametric form. The scene occupancy, on the other hand, is constructed using a grid map with a resolution of 0.2m, where each grid cell is labeled according to its movability status, characterized as non-parametric To encode upstream output for different usages, we design representations for scene and instance levels, which are applied to trajectory evaluation and generation respectively.

**Scene Representation** We adopt rasterization proposed by [9] for scene representation. Scene rasterization with convolutional forwarding can better capture scene-level cues compared to instance vectorization, avoiding information loss to the maximum extent. Owing to the convolutional network’s property of exploiting spatially local correlation, undefined or irregular elements like construction areas, traffic cones, and roadblocks can be incorporated with a unified design regardless of how they are organized and whether they have regularized shapes. Additional scene information depicted by free space or occupancy, lacking parametric description, can hardly be involved with vectorized representation and, once omitted, can be fatal to safety-critical systems. To serve as a qualified trajectory evaluator, BEV rasterization involves environment cues from online perception outputs as much as possible to capture those ”devils in detail”. We follow the interpretable design as that of in [3], but rasterize different scene elements(e.g. agent, lanes, occupancy, route) into different binary channels to enable reasoning about the distinct element separately. The details can be found in our appendix.

**Instance Representation** The instance representation is employed to address the shortcomings of scene encoding, which are afflicted by the truth that, rasterization is prone to distorting highly organized and structured information, rendering it disorganized. Since this procedure is irreversible, making it challenging to retrieve instance encoding for lane center lines, road boundaries, and other elements. The vectorized representation combined with the transformer has been proven to be superior to CNN forwarding on BEV raster in terms of accuracy and efficiency [13] for the motion prediction task. To take advantage of modeling in such form, we adopt vectorization [13] to encode the perception outputs into vector sets. Instances with parametric descrip-

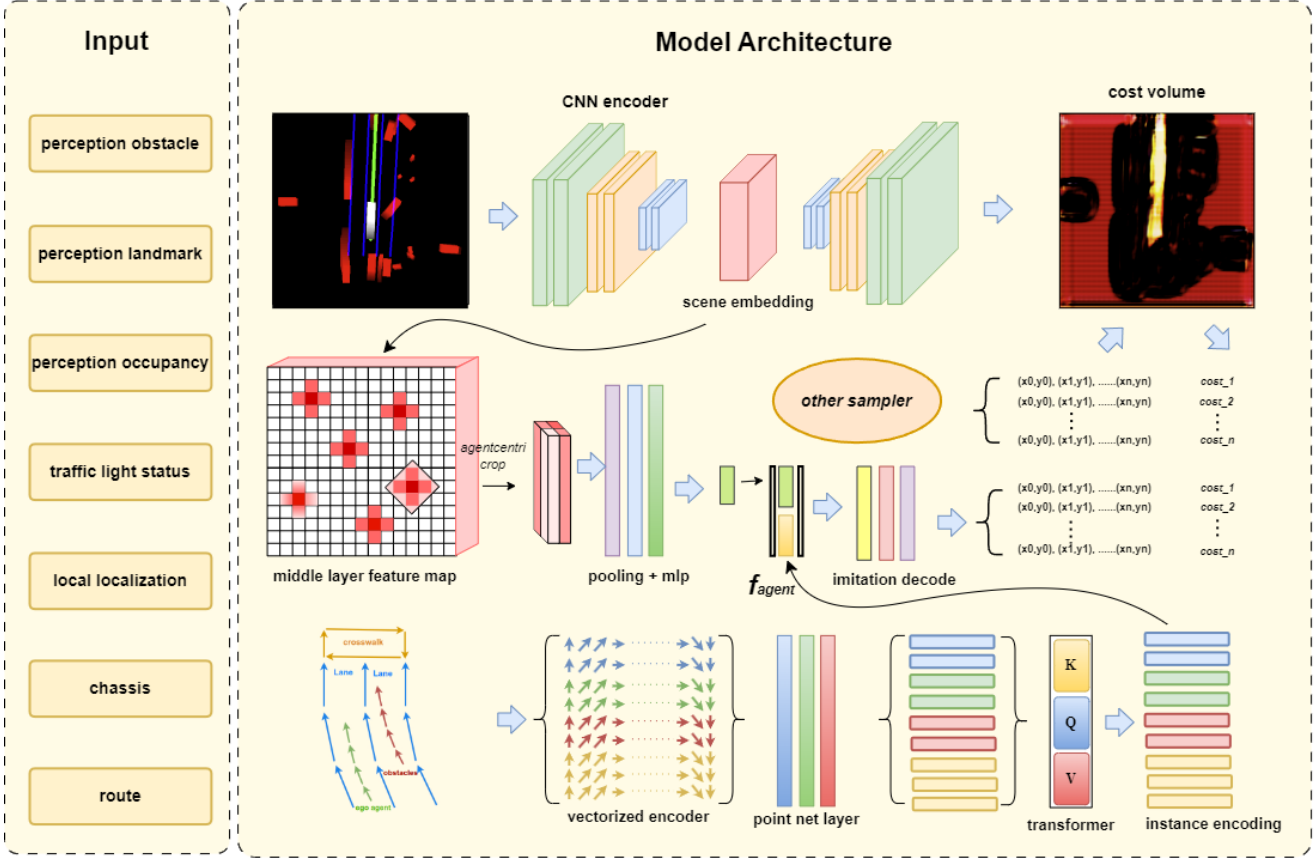


Figure 1. Model Structure of GAD. The model initiates with two streams for rasterization and vectorization respectively to encode scene and instance-level features. The rasterization branch utilize convolution layers to derive the scene embedding, which is then decoded into cost volumes for scoring candidate trajectories from multiple samplers and prediction grid maps for agent prediction. Meanwhile the scene embedding are cropped and incorporated with the instance encoding from vectorization branch to decode agents’ future movements.

tion are encoded in the vector form, including route points, ego and agent historical, lane center lines, and road boundaries, while non-parametric outputs are ignored, like occupancy, construction area, roadblocks, and other irregular elements. Each element includes position and type features, with the position described relative to the SDV pose. The relationships between separated elements are organized as a graph.

### 3.2. Model Structure

We build a multi-resolution, two-stream backbone network to encode inputs and extract agents and scene features separately. As shown in Fig. 1. One steam processes the rasterized scene while the other deals with the vectorized graph. As for scene encoding, we build a convolutional encoder composed of several residual blocks with corresponding layers and strides. Namely, the features after each block are down-sampled accordingly from the input in the BEV raster to obtain the scene embedding. The rasterization branch has more layers than the vectorization branch

as the input is much denser than the vectorized graph. This stream is responsible for aggregating geometric information from the scene context to extract global appearance and motion cues. After obtaining scene embedding from the CNN encoder, it is passed through two separate decoders with identical structures but different purposes. Both decoders are composed of deconvolution layers to restore the output to the same size as the rasterization input. The first decoder outputs the cost volume while the other outputs the predicted grid map. Both will be illustrated in the next section.

Meanwhile, in the other stream, inspired by [13], the instance-level encoding is built on a hierarchical graph network-based architecture. It consists of a PointNet-based [34] local sub-graph for processing local information from vectorized inputs and a global graph using a Transformer encoder [43] for reasoning about interactions over agents and landmark features.

Finally, the corresponding scene encoding for the agent is obtained via oriented crop [4] in ego-centric mid-level



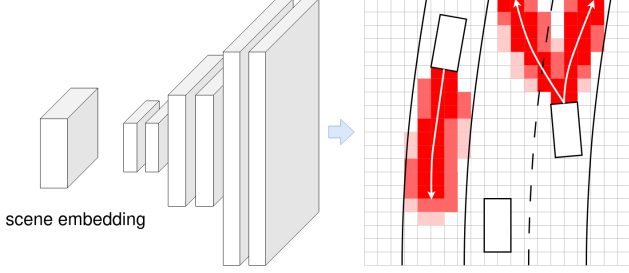


Figure 2. Multi-stage Prediction

feature and fused with instance encoding by concatenation along the feature dimension which outputs high-dimensional tensors  $f_{agent}$ . With the agent-level embeddings, an imitation decoder is utilized to output the predicted trajectories per agent. The details for the encoder and decoders are illustrated in the appendix.

### 3.3. Route

When HD maps are accessible, the input route is typically given in the form of a sequence of lanes that the SDV should follow. In HD map-free settings, however, this is not possible, especially for turning scenarios in intersections where no leading landmark is available. In our mapless setting, route information is derived from visual landmark and human commuting trajectories for different scenarios to substitute those absent cues. The lane center lines constructed by landmarks are mainly used in cruise and lane change scenarios, while in turning scenarios, the starting and ending positions are recorded in advance, once vehicles approach the intersection, the human commuting trajectories will serve as route. More details can be found in the appendix.

### 3.4. Prediction

We follow a multi-stage design for scene and agent prediction. In the first stage, the pipeline aims to predict the scene level grid map, also known as the heat map or occupancy. We regress a grid map  $G_{ij}^t = dec(f_{ras})$  with a resolution matches that of the rasterization input by decoding the middle layer features.

The decoder, as mentioned in 3.2, shared an identical design as that of for cost volume but with the supervision from the rasterization of the agents' future ground truth box. This grid is trained with pixel-wise focal loss inspired from [15]:

$$L_{occ.pred} = - \sum_{ij} [\tilde{g}_{ij}(1 - \hat{g}_{ij})^2 \log(\hat{g}_{ij}) + (1 - \tilde{g}_{ij})\hat{g}_{ij}^2 \log(1 - \hat{g}_{ij})] \quad (1)$$

Here,  $\tilde{g}_{ij}$  represents the class label for the grid, where  $\tilde{g}_{ij} = 1$  indicates that it is occupied.

In the second stage, the model forecasts agent-level trajectories with the scene prior from the predicted grid. For the agent-level prediction, we follow the interactive design. Since the output trajectories are mainly adopted in sampling for SDV's following and overtaking, we only capture nearby agents and assume they will interact with the ego. In particular, we gather the corresponding probability of nearby landmarks by accumulating grid probability belonging to those areas, filtering out the candidates with higher results as the target prior. Those landmarks indicate areas where interaction is most likely to happen. The agents' trajectories will be decoded conditioned on that lane prior:

$$Traj = dec(f_{agent}|f_{lane}) \quad (2)$$

Here,  $f_{agent}$  is the instance encoding as illustrated in Sec. 3.2,  $f_{lane}$  is the corresponding lane encoding obtained in the same way. For the training phase, the ground truth  $\tilde{lane}$  corresponding to the agent's future trajectory will be labeled and incorporated as a condition prior:

$$L_{traj.pred} = L2(Traj, dec(f_{agent}|f_{\tilde{lane}})) \quad (3)$$

The training loss is measured by the  $L2$  distance between the predicted and ground truth trajectory.

### 3.5. Trajectory Evaluation

The previous section described a method for multi-stage prediction that outputs grid maps and interactive trajectories. We now show that such grid maps combined with perception occupancy can be integrated directly into an end-to-end motion planner that makes use of space-time cost maps for scoring candidate trajectories. We follow [48] in max-margin planning, but modify their derivation to take into account scene occupancy and predicted grid map. Our evaluator decodes a space-time cost map  $C_{xy}^t = dec(f_{ras})$  in grid form over future timestamps given BEV raster. The cost of a trajectory is defined as the sum of costs at its space-time way-points. The best candidate trajectory is the one with the lowest cost according to the learned cost:

$$s = arg \min_{\hat{s} \in S} \sum_t [C(\hat{s}) + \alpha O_{cc}(\hat{s}) + \beta G_{rid}(\hat{s})] \quad (4)$$

where  $S$  represents the set of viable future trajectories,  $O_{cc}$  represents perception occupancy,  $G_{rid}$  is the predicted grid map,  $\alpha$  and  $\beta$  are the weights respectively. Since selecting the minimum-cost trajectory within a discrete set is not differentiable, we use the max-margin loss to penalize trajectories that have small cost and are different from the human driving trajectory or are unsafe. Let  $\hat{s}$  and  $\tilde{s}$  be the input and human trajectory respectively for a given example. We utilize the max-margin loss to encourage the human driving trajectory to have a smaller cost than other trajectories.

$$L_{cost.volume} = \max_{\tilde{s}} [C(\tilde{s}) - C(\hat{s}) + Diff(\tilde{s}, \hat{s})] \quad (5)$$

The *Diff* value here serves as compensation to quantitatively measure the difference between the human demonstrated and our candidates. It has to tell how goodness of the human driving or how badness of our samplers, quantified by planning targets, avoiding static collisions, and managing dynamic interactions, etc. So that the evaluator can assign comparable costs to the trajectories in our candidate set. In particular:

$$Diff(\tilde{s}, \hat{s}) = L2(\tilde{s}, \hat{s}) + O(\hat{s}) + G(\hat{s}) \quad (6)$$

where  $O$  is the occupancy cost,  $G$  is the rest of the prediction costs as defined in Sec. 3.4. The imitation loss  $L2$  measures the  $l2$  distance between trajectory  $\hat{s}$  and the ground-truth  $\tilde{s}$  for the entire horizon.

### 3.6. Trajectory Generation

Given the learned cost volume, the final trajectory can then be computed by minimizing Eq. (4). Note, however, that this optimization with physical constraints is NP-hard. On one hand, we evaluate and extend previous works on trajectory sampling [3, 21, 38, 48] with a more sophisticated design by incorporating prior knowledge and structured outputs from perception and prediction. Furthermore, we leverage a GAN-based pipeline during the generator’s training to solve the optimization problem. In this section, we describe our sampling and generation algorithm.

The sampling and generating algorithms can be mainly categorized into reference line-based and reference line-free. Methods incorporating reference information can generate long-term consistent outputs in the loops. Since this information rarely changes over time, bridging consecutive frames promotes cross-frame stability. However, scenarios still need to be handled where reference-related information can hardly be obtained. To enhance the scalability of our system, we consider trajectory from the following methods. In our implementation, curve and retrieval-based samplers are reference line-free, while the others rely on reference information constructed by visual landmarks or commuting trajectories.

**Curve Based Sampler** As the most basic sampler, it has been adopted by a few previous methods [48]. We follow [48] with little modifications for comfort concerns. We take into account the initial states of a Self-Driving Vehicle (SDV), such as velocity, acceleration, heading, and road curvature where the SDV is located, and then sample a combination of straight lines, circles, and clothoid curves as trajectories with the given initial states and random end states within a pre-defined range. The curve-based sampler serves as the baseline sampling algorithm in our experiment. The details can be found in the appendix.

**Retrieval Based Sampler** Following prior work that uses data-driven trajectory sampling techniques in mapless driving scenarios [3], we create an expert trajectory dataset by clustering manual driving data. Once this dataset is constructed during pre-processing, SDV can retrieve trajectories with high similarity according to its current motion states. The construction and retrieval details can be found in the appendix.

**Lattice Sampler** Qi added The lane centers and surrounding agents’ movements are strong priors to construct the potential trajectory to be executed by the SDV. When landmarks are available, the lane geometry can be exploited to guide the trajectory sampling process. The predicted trajectory, on the other hand, can be incorporated to generate interactive behavior like following or overtaking in longitude. In our paradigm, they are both available as depicted by Sec. 3.4 Sec. 3.1. In particular, we follow the trajectory parameterization and sampling philosophy proposed in [39, 45]. Our sampled trajectories consist of lane keep, lane change, nudge, side pass in lateral, and follow, overtake, yield, stop in longitude. We illustrate the detail in the appendix.

**Imitation Planner** For the imitation planner, previous approaches choose to mimic a human driver with one single trajectory [22, 24]. But such designs suffer from model collapse in both longitude and lateral. Owing to our generator-evaluator paradigm, we can generate a bunch of diverse candidates and pass them to the downstream evaluation task. We follow multiple-trajectory [8] design in trajectory prediction to estimate the conditional distribution  $P(S|f_{plan})$  in motion planning task. Where  $S = [\hat{s}_1, \dots, \hat{s}_m]$  is the trajectories with  $m$  different maneuvers such as lane following, lane changing, agent following, agent overtaking.  $f_{plan}$  stands for feature prepared for planning task.  $\parallel$  stands for concatenation.

$$f_{plan} = [f_{scene} \parallel f_{route} \parallel f_{SDV}] \quad (7)$$

$$P(S|f_{plan}) = \sum_M P(S|m, f_{plan})P(m|f_{plan}) \quad (8)$$

Our imitation generator decodes a multitude of  $M$  possible trajectories for ego move in local coordinates.

$$[\hat{s}_1, \dots, \hat{s}_m] = G(f_{plan}) \quad (9)$$

During the training phase, we then identify mode  $m^*$  that is closest to the ground-truth trajectory according to distance function,

$$L_{imit.plan} = arg \min_{i \in 1, \dots, m} dist(\tilde{s}, \hat{s}_i) \quad (10)$$

We select  $L2$  dist for the distance function.

**GAN Based Planner** The above imitation generator is trained separately from our evaluator by different headers. With the attempt to generate trajectory with minimal cost, we propose a GAN base planner with modification to the training paradigm that bridges the isolated optimization targets, so that Eq. (4) can be solved by learning. For standard adversarial loss [16], also known as the min-max loss, the generator tries to minimize below function while the discriminator tries to maximize it.

$$L_{gan} = \min_G \max_D (E_x[\log(D(x))] + E_z[\log(1 - D(G(z)))]) \quad (11)$$

$\log(D(x))$  refers to the probability that the discriminator is rightly classifying the real case, maximizing  $\log(1 - D(G(z)))$  would help it to label the fake sample that comes from the generator correctly. In our paradigm, we replace the discriminator with an evaluator. But different from the standard discriminator in GAN, which gives qualitative labels that indicate true or false, our evaluator output score to measure the discrepancy between candidates quantitatively. So the optimization target for evaluator Eq. (5) still holds, but the learning target of the imitation planner becomes:

$$L_{generator} = E(G(m)) + Diff(\tilde{s}, G(m)) \quad (12)$$

$$L_{evaluator} = \max_{\hat{s}} [E(\tilde{s}) - E(\hat{s}) + Diff(\tilde{s}, \hat{s})] \quad (13)$$

with:

$$E(s) = C(s) = \sum_{(x_t, y_t) \in s} C(x_t, y_t) \quad (14)$$

$$C_{xy}^t = dec(f_{ras}) \quad (15)$$

$$G(m) = \hat{S} = [\hat{s}_1, \dots, \hat{s}_m] \quad (16)$$

Here  $m$  is an hidden variable represent the manual in planning.

### 3.7. Safety layer

For on-road autonomous driving motion planning, a strategy for safety coverage is necessary. The perception occupancy and trajectory prediction results are used to validate the trajectory candidates with respect to safety. The trajectory prepared for the safety layer is a little bit different to Eq. (2) in that no prior is assumed in decoding. We sort the trajectories according to the evaluated costs and iterate them to check the basic rule in modularized form (like trajectory and bounding box) until we cache enough candidates by ascending order. To ensure cross-frame consistency, we reserve  $n$  validated trajectories with the lowest cost and compare them with planning output in the last frame. The above objective promotes the system’s robustness with respect to the corner cases that our model fails to handle. We believe such a layer of safety guarantee is indispensable for manufacturing our system at scale.

## 4. Experiments

We construct different baseline variants of our models in both open-loop and closed-loop for ablative studies and compare them with state-of-the-art alternative methods quantitatively. We gather in-house datasets for training and open-loop settings. It contains a wide range of driving scenarios in a densely populated urban environment. We collected the record files in 15 hours, which captured the perception output, the SDV trajectory, and route info. All the records are post-processed to obtain 200k clips in total. By default, we take the 1.5s of past context and predict/plan the future 3.0s contexts, corresponding to 15 frames in the past and 30 frames in the future. We partition the dataset into 16w for training and 4w for testing. To validate the potential of our method, we disable the functionality in the safety layer as well as the optimizer and safety backup subsystem in other methods. More details on protocols are provided in the appendix.

### 4.1. Prediction

We focus on the  $L2$  distance and hit rate for the open-loop prediction. Preview SOTAs are evaluated in our HD map-free setting.

### 4.2. Open-loop Planning

For the open-loop planning, we focus on two evaluation metrics:  $L2$  error and collision rate, and align the planning horizon to 3.0s for a fair comparison. We compute the  $L2$  error between the planned trajectory and the human driving trajectory, and evaluate how often the SDV would collide with other agents on the road. Detailed comparison with previous methods is shown in Tab. Note that the Vanilla algorithm is penalized based on how much the trajectory deviates from the ground truth, thus it achieves the lowest  $L2$  error but largest collision rates in all prediction horizons.

### 4.3. Closed-loop Experimental

We first evaluate the necessity of different sampler on closed-loop simulation by ablation study. Then, find the best combination to evaluate in the real-world. The results of ablation study illustrated appendix.

We extensively tested andn appendix. compare the above methods in the real world, in densely populated urban area, under the supervision of human safety drivers. The driving route used for our experiments is shown on appendix. During the 100+ mile public road testing, the model successfully performed a wide variety of challenging maneuvers including lane-following, merging, yielding to pedestrians or nudging around parked cars.

## 5. Conclusions

## 6. Acknowledgements

We would like to thank the following contributors who work on the toolchains to support our closed-loop evaluation and onboard road test: Chi.Zhang, Yue.Li, Bolin.Zhao, Yanze.Liu, Liang.Zhu.

## References

- [1] Mariusz Bojarski, Davide Del Testa, Daniel Dworakowski, Bernhard Firner, Beat Flepp, Praseon Goyal, Lawrence D Jackel, Mathew Monfort, Urs Muller, Jiakai Zhang, et al. End to end learning for self-driving cars. *arXiv preprint arXiv:1604.07316*, 2016. [3](#)
- [2] Sergio Casas, Cole Gulino, Simon Suo, and Raquel Urtasun. The importance of prior knowledge in precise multimodal prediction. In *2020 IEEE/RSJ International Conference on Intelligent Robots and Systems (IROS)*, pages 2295–2302. IEEE, 2020. [2](#)
- [3] Sergio Casas, Abbas Sadat, and Raquel Urtasun. Mp3: A unified model to map, perceive, predict and plan. In *Proceedings of the IEEE/CVF Conference on Computer Vision and Pattern Recognition*, pages 14403–14412, 2021. [1](#), [3](#), [6](#), [11](#)
- [4] Yuning Chai, Benjamin Sapp, Mayank Bansal, and Dragomir Anguelov. Multipath: Multiple probabilistic anchor trajectory hypotheses for behavior prediction. *arXiv preprint arXiv:1910.05449*, 2019. [2](#), [4](#)
- [5] Felipe Codevilla, Matthias Müller, Antonio López, Vladlen Koltun, and Alexey Dosovitskiy. End-to-end driving via conditional imitation learning. In *2018 IEEE international conference on robotics and automation (ICRA)*, pages 4693–4700. IEEE, 2018. [3](#)
- [6] Felipe Codevilla, Eder Santana, Antonio M López, and Adrien Gaidon. Exploring the limitations of behavior cloning for autonomous driving. In *Proceedings of the IEEE/CVF international conference on computer vision*, pages 9329–9338, 2019. [3](#)
- [7] Alexander Cui, Sergio Casas, Abbas Sadat, Renjie Liao, and Raquel Urtasun. Lookout: Diverse multi-future prediction and planning for self-driving. In *Proceedings of the IEEE/CVF International Conference on Computer Vision*, pages 16107–16116, 2021. [1](#), [3](#)
- [8] Henggang Cui, Vladan Radosavljevic, Fang-Chieh Chou, Tsung-Han Lin, Thi Nguyen, Tzu-Kuo Huang, Jeff Schneider, and Nemanja Djuric. Multimodal trajectory predictions for autonomous driving using deep convolutional networks. In *2019 international conference on robotics and automation (icra)*, pages 2090–2096. IEEE, 2019. [2](#), [6](#)
- [9] Nemanja Djuric, Vladan Radosavljevic, Henggang Cui, Thi Nguyen, Fang-Chieh Chou, Tsung-Han Lin, Nitin Singh, and Jeff Schneider. Uncertainty-aware short-term motion prediction of traffic actors for autonomous driving. In *Proceedings of the IEEE/CVF Winter Conference on Applications of Computer Vision*, pages 2095–2104, 2020. [3](#)
- [10] Alexey Dosovitskiy, German Ros, Felipe Codevilla, Antonio Lopez, and Vladlen Koltun. Carla: An open urban driving simulator. In *Conference on robot learning*, pages 1–16. PMLR, 2017. [2](#)
- [11] Alberto Elfes. Using occupancy grids for mobile robot perception and navigation. *Computer*, 22(6):46–57, 1989. [3](#)
- [12] Alberto Elfes. Occupancy grids: A stochastic spatial representation for active robot perception. *arXiv preprint arXiv:1304.1098*, 2013. [1](#)
- [13] Jiyang Gao, Chen Sun, Hang Zhao, Yi Shen, Dragomir Anguelov, Congcong Li, and Cordelia Schmid. Vectornet: Encoding hd maps and agent dynamics from vectorized representation. In *Proceedings of the IEEE/CVF Conference on Computer Vision and Pattern Recognition*, pages 11525–11533, 2020. [3](#), [4](#)
- [14] Kyle Gao, Yina Gao, Hongjie He, Dening Lu, Linlin Xu, and Jonathan Li. Nerf: Neural radiance field in 3d vision, a comprehensive review. *arXiv preprint arXiv:2210.00379*, 2022. [2](#)
- [15] Thomas Gilles, Stefano Sabatini, Dzmitry Tsishkou, Bogdan Stanculescu, and Fabien Moutarde. Home: Heatmap output for future motion estimation. In *2021 IEEE International Intelligent Transportation Systems Conference (ITSC)*, pages 500–507. IEEE, 2021. [5](#)
- [16] Ian Goodfellow, Jean Pouget-Abadie, Mehdi Mirza, Bing Xu, David Warde-Farley, Sherjil Ozair, Aaron Courville, and Yoshua Bengio. Generative adversarial networks. *Communications of the ACM*, 63(11):139–144, 2020. [7](#)
- [17] Agrim Gupta, Justin Johnson, Li Fei-Fei, Silvio Savarese, and Alexandre Alahi. Social gan: Socially acceptable trajectories with generative adversarial networks. In *Proceedings of the IEEE conference on computer vision and pattern recognition*, pages 2255–2264, 2018. [2](#)
- [18] Stefan Hoermann, Martin Bach, and Klaus Dietmayer. Dynamic occupancy grid prediction for urban autonomous driving: A deep learning approach with fully automatic labeling. In *2018 IEEE International Conference on Robotics and Automation (ICRA)*, pages 2056–2063. IEEE, 2018. [3](#)
- [19] Joey Hong, Benjamin Sapp, and James Philbin. Rules of the road: Predicting driving behavior with a convolutional model of semantic interactions. In *Proceedings of the IEEE/CVF Conference on Computer Vision and Pattern Recognition*, pages 8454–8462, 2019. [3](#)
- [20] Anthony Hu, Gianluca Corrado, Nicolas Griffiths, Zachary Murez, Corina Gurau, Hudson Yeo, Alex Kendall, Roberto Cipolla, and Jamie Shotton. Model-based imitation learning for urban driving. *Advances in Neural Information Processing Systems*, 35:20703–20716, 2022. [1](#), [2](#), [3](#)
- [21] Shengchao Hu, Li Chen, Penghao Wu, Hongyang Li, Junchi Yan, and Dacheng Tao. St-p3: End-to-end vision-based autonomous driving via spatial-temporal feature learning. In *European Conference on Computer Vision*, pages 533–549. Springer, 2022. [1](#), [2](#), [3](#), [6](#)
- [22] Yihan Hu, Jiazhi Yang, Li Chen, Keyu Li, Chonghao Sima, Xizhou Zhu, Siqi Chai, Senyao Du, Tianwei Lin, Wenhai Wang, et al. Planning-oriented autonomous driving. In *Proceedings of the IEEE/CVF Conference on Computer Vision and Pattern Recognition*, pages 17853–17862, 2023. [1](#), [2](#), [6](#)



- [23] Ajay Jain, Sergio Casas, Renjie Liao, Yuwen Xiong, Song Feng, Sean Segal, and Raquel Urtasun. Discrete residual flow for probabilistic pedestrian behavior prediction. In *Conference on Robot Learning*, pages 407–419. PMLR, 2020. 3
- [24] Bo Jiang, Shaoyu Chen, Qing Xu, Bencheng Liao, Jiajie Chen, Helong Zhou, Qian Zhang, Wenyu Liu, Chang Huang, and Xinggang Wang. Vad: Vectorized scene representation for efficient autonomous driving. In *Proceedings of the IEEE/CVF International Conference on Computer Vision*, pages 8340–8350, 2023. 1, 2, 3, 6
- [25] Alex Kendall, Jeffrey Hawke, David Janz, Przemyslaw Mazur, Daniele Reda, John-Mark Allen, Vinh-Dieu Lam, Alex Bewley, and Amar Shah. Learning to drive in a day. In *2019 international conference on robotics and automation (ICRA)*, pages 8248–8254. IEEE, 2019. 1, 3
- [26] Namhoon Lee, Wongun Choi, Paul Vernaza, Christopher B Choy, Philip HS Torr, and Manmohan Chandraker. Desire: Distant future prediction in dynamic scenes with interacting agents. In *Proceedings of the IEEE conference on computer vision and pattern recognition*, pages 336–345, 2017. 2
- [27] Quanyi Li, Zhenghao Peng, Lan Feng, Qihang Zhang, Zhenghai Xue, and Bolei Zhou. Metadrive: Composing diverse driving scenarios for generalizable reinforcement learning. *IEEE Transactions on Pattern Analysis and Machine Intelligence*, 2022. 2
- [28] Zhiqi Li, Zhiding Yu, Shiyi Lan, Jiahao Li, Jan Kautz, Tong Lu, and Jose M Alvarez. Is ego status all you need for open-loop end-to-end autonomous driving? *arXiv preprint arXiv:2312.03031*, 2023. 2
- [29] Ming Liang, Bin Yang, Rui Hu, Yun Chen, Renjie Liao, Song Feng, and Raquel Urtasun. Learning lane graph representations for motion forecasting. In *Computer Vision–ECCV 2020: 16th European Conference, Glasgow, UK, August 23–28, 2020, Proceedings, Part II 16*, pages 541–556. Springer, 2020. 3
- [30] Matthias Müller, Alexey Dosovitskiy, Bernard Ghanem, and Vladlen Koltun. Driving policy transfer via modularity and abstraction. *arXiv preprint arXiv:1804.09364*, 2018. 3
- [31] Brian Paden, Michal Čáp, Sze Zheng Yong, Dmitry Yershov, and Emilio Frazzoli. A survey of motion planning and control techniques for self-driving urban vehicles. *IEEE Transactions on intelligent vehicles*, 1(1):33–55, 2016. 10
- [32] Tung Phan-Minh, Elena Corina Grigore, Freddy A Boulton, Oscar Beijbom, and Eric M Wolff. Covernet: Multimodal behavior prediction using trajectory sets. In *Proceedings of the IEEE/CVF conference on computer vision and pattern recognition*, pages 14074–14083, 2020. 2
- [33] Dean A Pomerleau. Alvin: An autonomous land vehicle in a neural network. *Advances in neural information processing systems*, 1, 1988. 3
- [34] Charles R Qi, Hao Su, Kaichun Mo, and Leonidas J Guibas. Pointnet: Deep learning on point sets for 3d classification and segmentation. In *Proceedings of the IEEE conference on computer vision and pattern recognition*, pages 652–660, 2017. 4
- [35] Katrin Renz, Kashyap Chitta, Otniel-Bogdan Mercea, A Koepke, Zeynep Akata, and Andreas Geiger. Plant: Explainable planning transformers via object-level representations. *arXiv preprint arXiv:2210.14222*, 2022. 3
- [36] Nicholas Rhinehart, Kris M Kitani, and Paul Vernaza. R2p2: A reparameterized pushforward policy for diverse, precise generative path forecasting. In *Proceedings of the European Conference on Computer Vision (ECCV)*, pages 772–788, 2018. 2
- [37] Daniela Ridel, Nachiket Deo, Denis Wolf, and Mohan Trivedi. Scene compliant trajectory forecast with agent-centric spatio-temporal grids. *IEEE Robotics and Automation Letters*, 5(2):2816–2823, 2020. 3
- [38] Abbas Sadat, Sergio Casas, Mengye Ren, Xinyu Wu, Pranaab Dhawan, and Raquel Urtasun. Perceive, predict, and plan: Safe motion planning through interpretable semantic representations. In *Computer Vision–ECCV 2020: 16th European Conference, Glasgow, UK, August 23–28, 2020, Proceedings, Part XXIII 16*, pages 414–430. Springer, 2020. 1, 3, 6
- [39] Abbas Sadat, Mengye Ren, Andrei Pokrovsky, Yen-Chen Lin, Ersin Yumer, and Raquel Urtasun. Jointly learnable behavior and trajectory planning for self-driving vehicles. in 2019 iee. In *RSJ International Conference on Intelligent Robots and Systems (IROS)*, pages 3949–3956. 6
- [40] Hao Shao, Letian Wang, Ruobing Chen, Hongsheng Li, and Yu Liu. Safety-enhanced autonomous driving using interpretable sensor fusion transformer. In *Conference on Robot Learning*, pages 726–737. PMLR, 2023. 1, 2
- [41] Charlie Tang and Russ R Salakhutdinov. Multiple futures prediction. *Advances in neural information processing systems*, 32, 2019. 2
- [42] Sebastian Thrun. Learning occupancy grid maps with forward sensor models. *Autonomous robots*, 15:111–127, 2003. 3
- [43] Ashish Vaswani, Noam Shazeer, Niki Parmar, Jakob Uszkoreit, Llion Jones, Aidan N Gomez, Łukasz Kaiser, and Illia Polosukhin. Attention is all you need. *Advances in neural information processing systems*, 30, 2017. 4
- [44] Matt Vitelli, Yan Chang, Yawei Ye, Ana Ferreira, Maciej Wołczyk, Błażej Osiński, Moritz Niendorf, Hugo Grimmer, Qiangui Huang, Ashesh Jain, et al. Safeynet: Safe planning for real-world self-driving vehicles using machine-learned policies. In *2022 International Conference on Robotics and Automation (ICRA)*, pages 897–904. IEEE, 2022. 3
- [45] Moritz Werling, Julius Ziegler, Sören Kammel, and Sebastian Thrun. Optimal trajectory generation for dynamic street scenarios in a frenet frame. In *2010 IEEE international conference on robotics and automation*, pages 987–993. IEEE, 2010. 6
- [46] Pengxiang Wu, Siheng Chen, and Dimitris N Metaxas. Motionnet: Joint perception and motion prediction for autonomous driving based on bird’s eye view maps. In *Proceedings of the IEEE/CVF conference on computer vision and pattern recognition*, pages 11385–11395, 2020. 3
- [47] Penghao Wu, Xiaosong Jia, Li Chen, Junchi Yan, Hongyang Li, and Yu Qiao. Trajectory-guided control prediction for end-to-end autonomous driving: A simple yet strong baseline. *Advances in Neural Information Processing Systems*, 35:6119–6132, 2022. 2

- [48] Wenyuan Zeng, Wenjie Luo, Simon Suo, Abbas Sadat, Bin Yang, Sergio Casas, and Raquel Urtasun. End-to-end interpretable neural motion planner. In *Proceedings of the IEEE/CVF Conference on Computer Vision and Pattern Recognition*, pages 8660–8669, 2019. **1, 3, 5, 6**
- [49] Wenyuan Zeng, Shenlong Wang, Renjie Liao, Yun Chen, Bin Yang, and Raquel Urtasun. Dsdnet: Deep structured self-driving network. In *Computer Vision–ECCV 2020: 16th European Conference, Glasgow, UK, August 23–28, 2020, Proceedings, Part XXI 16*, pages 156–172. Springer, 2020. **1, 3**
- [50] Tianyang Zhao, Yifei Xu, Mathew Monfort, Wongun Choi, Chris Baker, Yibiao Zhao, Yizhou Wang, and Ying Nian Wu. Multi-agent tensor fusion for contextual trajectory prediction. In *Proceedings of the IEEE/CVF conference on computer vision and pattern recognition*, pages 12126–12134, 2019. **2**

## A. Appendix

### A.1. Scene Rasterization

The state of landmarks and road-bound is rasterized in the same channels, facilitating traffic flow reasoning at intersections. Each historical actor polygon is rasterized in the same channel as the current polygon but with a reduced brightness level, resulting in the fading effect. To distinct SDV from other agents, we rasterize ego’s polygon in an isolated channel, as well as it’s fading history. The rasterized map contains a rendering of traffic light permissibility in junctions, but we tackle it a little bit trick to handle the robustness. we render permitted (green light), yield (unprotected), or prohibited (red light ) by masking stop line with a static agent’s polygone that exhibit permissibilit of current ego route. Since we explore route from different source, we cast different routing form into one single uniformed \*\*\* All in all, we obtain a 3D tensor of size (Ha , Wa ,C), with C=5 binary channels for the map.

### A.2. Instance Vectorization

### A.3. Model Structure

### A.4. Route

As indicated previously, the route plays a critical role in guiding SDVs along roadways. Our route information comes from two primary channels: the lane center line and historical commuting trajectories.

The lane center lines, which can be accessed in perception channels, are mainly utilized for cruising scenarios, as the SDV consistently travels along the middle of the lane, and if it deviates from the center, it will be guided back to avoid hazards from adjacent lanes.

However, in lane-changing scenarios, vehicles move across lane markers, making the lane center line ineffective in determining optimal positions for lane changes. Consequently, historical commuting trajectories are utilized to

capture the lane-change starting and ending positions. Upon reaching the lane-change starting position or during the lane-change process, the collected trajectory supersedes the center line as the route, providing guidance for the SDV to change lanes.

Likewise, in turning scenarios, the absence of landmarks without HD-maps results in the SDV lacking appropriate instructions to navigate intersections. To address this, the starting and ending positions for turning are recorded. As the SDV approaches intersections, human-driving trajectories are employed as the route to guide the SDV through the intersections.

### A.5. Curve Based Sampler

In this appendix, we present the sampling procedure with more details. Vehicle trajectories can be categorized into two primary types: straight and turning. And turning trajectories encompass lane changes and turning at intersections. Lane-changing trajectories are characterized by variable curvature over time, while turning at intersections follows circular-like curves. As straight lines can be treated as a special case of curves, we introduce the curve-based sampler that focuses on generating straight, constant curvature circle-like, and variable curvature clothoid-like trajectories.

For straight ones, a sequence of acceleration values are sampled to account for various velocity-changing scenarios, which are subsequently integrated over time to obtain speed profiles. With initial states(the position and heading angle) of the autonomous vehicle, a set of straight trajectories can be obtained.

Circle trajectories employ the bicycle model [31] to establish the relationship between steering angle  $\phi$  and path curvature  $\kappa$ , represented by the formula  $\kappa = 2\tan(\phi)/L \approx 2\phi/L$ , where  $L$  is the distance between the front and rear axles of the autonomous vehicle. Using a constant curvature and different sampled speed profiles, a set of circle trajectories can be derived.

Clothoid curves involve a proportional relationship between the curvature  $\kappa$  of a point and its distance to the original point  $\xi$ , which can be defined as

$$\mathbf{s}(\xi) = \mathbf{s}_0 + a \left[ C \left( \frac{\xi}{a} \right) \mathbf{T}_0 + S \left( \frac{\xi}{a} \right) \mathbf{N}_0 \right] \quad (1)$$

$$C(\xi) = \int_0^\xi \cos \left( \frac{\pi u^2}{2} \right) du \quad (2)$$

$$S(\xi) = \int_0^\xi \sin \left( \frac{\pi u^2}{2} \right) du \quad (3)$$

Where  $\mathbf{s}(\xi)$  is the clothoid curve,  $\mathbf{T}_0$  and  $\mathbf{N}_0$  are the tangent and normal vector of point  $\mathbf{s}_0$ ,  $S(\xi)$  and  $C(\xi)$  are associated coefficients and defined as the Fresnel integral.

As the shapes of clothoid curves solely determined by the scaling factor  $a$ , we can generate a variety of clothoid trajectories by considering a suitable range for  $a$ , in combination with the initial curvature obtained from the bicycle model and the speed profiles.

### A.6. Lattice Sampler

The lattice sampler is a reference line-based method used to acquire multiple candidate trajectories along the reference line, taking into account future movements of surrounding obstacles to avoid potential hazards.

To begin, this method involves sampling multiple candidate trajectories based on the Frenet Frame, where the smooth lane central line is projected to the S coordinate and its normal direction is the L coordinate. Trajectories are composed of longitudinal and lateral paths, with the longitudinal one described as the station and time, denoted as  $S = \{s(t)\}$ , and the lateral path described as the lateral station and longitudinal one denoted, denoted  $L = l(s)$ .

When sampling trajectories, given the initial state  $[s_0, s'_0, s''_0], [l_0, l'_0, l''_0]$  at time  $t_0$ , the end states  $[s_1, s'_1, s''_1], [l_1, l'_1, l''_1]$  at time  $t_1$  are sampled to cover cruising, following, overtaking and stopping maneuvers, and consequently fits polynomials.

As for cruising maneuvers, vehicles must adhere to a specific cruising speed by adjusting their acceleration and deceleration. Therefore a set of prediction time horizon  $t_1$  and end-condition longitudinal velocities  $s'_1$  are uniformly sampled within a pre-defined range of the cruising speed. This sampling process is facilitated by a quartic polynomial.

When it comes to stopping maneuvers, vehicles are obliged to come to a complete stop within a designated distance in order to comply with traffic signals or ensure a safe distance from stationary obstacles. In this scenario, the end states such as speed and accelerations are fixed at 0, while the prediction time  $t_1$  and end longitudinal distance  $s_1$  are sampled. These parameters are then described using a quintic polynomial.

Regarding following and overtaking maneuvers, these actions often arise when a preceding vehicle is moving at a slower pace or a new vehicle unexpectedly merges into a lane. The execution of these complex maneuvers is facilitated through the use of an s-t graph, which depicts the occupation of the lane by vehicles over time as illustrated in Figure x. By analyzing the s-t graph, end states can be sampled within unoccupied areas, marked in red (for overtaking) and blue (for following), thus facilitating the completion of these maneuvers through the use of a quintic polynomial.

Finally, these polynomials can be transformed back to Cartesian coordinate system to obtain the corresponding trajectories, which are consequently evaluated for compliance with kinematic constraints. If any trajectory does not

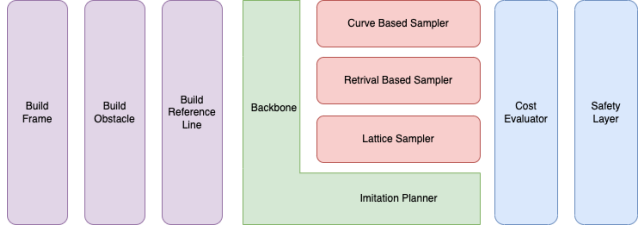


Figure 3. pipeline

meet the requirements, it will be removed from the sampling set.

### A.7. Retrieval-based Sampler

The retrieval based sampler does not depend on the map or lane information to generate trajectories, instead, it retrieves a cluster of trajectories whose initial state are close to the SDV's current state from a pre-established expert trajectory dataset.

To build the expert trajectory dataset, we utilized about 350 hours of driving trajectories from experienced human drivers. However, a substantial portion of the original human driving trajectories contains duplicate or very similar samples. Drawing inspiration from [3], we conducted subdivision and clustering on the original human driving trajectories in order to preserve diversity while simplifying the expert trajectory dataset.

To subdivide the original trajectories into different bins, we use the initial velocity  $v$ , acceleration  $a$  and curvature  $\kappa$ , with respective bin sizes of  $1.0 \frac{m}{s}$ ,  $0.5 \frac{m}{s^2}$ ,  $0.01 \frac{1}{m}$ . In each bins, trajectories are clustered into 2000 sets and the closest trajectory to each cluster center is retained. Finally, the trajectories from each subset will be aggregated to the comprehensive expert trajectory dataset.

Furthermore, we use kd-tree to organize the expert trajectory dataset to speed up the query and sampling of SDV. Each trajectory is constructed as a node in the k-d tree, with its initial state  $(v_0, a_0, \kappa_0)$  serving as the basis for the tree's partitioning.

When it comes to sampling, the current state of SDV will be used as a query vector  $\mathbf{q}=(v_{SDV}, a_{SDV}, \kappa_{SDV})$  to select trajectories from the k-d tree and the distance function for k-d tree nodes is defined as:

$$D = \beta_1 \cdot |v - v_{SDV}| + \beta_2 \cdot |a - a_{SDV}| + \beta_3 \cdot |\kappa - \kappa_{SDV}| \quad (1)$$

In this paper, we assign different weights to the differences in velocity  $v$ , acceleration  $a$  and curvature  $\kappa$ , with  $\beta_1 = 1.0$ ,  $\beta_2 = 5.0$ ,  $\beta_3 = 40.0$  and all nodes with  $D < 1.0$  will be added into output for the retrieval-based sampler.

### A.8. Hardware

Our autonomous driving algorithms have undergone rigorous testing on the recently launched Jiyue 01 vehicle,

whose detailed parameters can be found in the following link: <https://www.jiyue-auto.com/robocar-01>. The Jiyue 01 is equipped with a comprehensive sensor suite, which includes 11 cameras strategically positioned to provide front, side, rear, and surround-view coverage. Additionally, the vehicle features 5 millimeter-wave radars, enabling accurate perception in challenging weather conditions, and 12 ultrasonic radars for close-range detection.

Moreover, the Jiyue 01 is fitted with 2 NVIDIA Orin-X chips, representing a powerful and advanced autonomous driving hardware and software platform. Specifically engineered for autonomous driving, these chips offer a processing capability of 508 TOPS, meeting the high demands of algorithm design and ensuring optimal performance. More NVIDIA-Orin parameters can be found in the following link: <https://developer.nvidia.com/drive/agx>.

## A.9. Task Perf

## A.10. Road Test

Our road tests are conducted in the Jiading District of Shanghai, China, known for "Shanghai Automobile City". The detailed testing route is illustrated in Figure 4, encompassing straight stretches, lane changes, intersections, and turning scenes involving various traffic participants.

The route begins at No.1688 Yecheng Road, a road with two lanes in each direction, encounters frequent cars and electric bicycles. It passes through two intersections controlled by traffic lights before entering a three-lane structure and making a careful lane change to the right-most lane, where sometimes occupied by static vans. It then queues before the stop line and then turns onto Shengxin Road, a four-lane-per-direction road heavily congested commuter route with significant traffic flows in all directions.

While weaving through vehicles on Shengxin Road and go straight across the first intersection, the route carefully enters the right-most lane, and then turns right, encountering electric bicycles and vehicles from different directions at the intersection. After turning onto South Huicheng Road, a one lane per direction road often occupied by passengers and tricycles, the traffic flows are slowed down, requiring careful navigations.

The route then follows a right-turning at the next intersection and enters Huocheng Road, a narrow one-lane-per-direction road where trucks from the opposite direction sometimes encroaching on the ego lane, necessitating slight steering to avoid collisions. Proceeding through the next intersection, the route goes straight and executes an unprotected left turn to cross a bustling transportation route frequently used by trucks. Finally, the route circles back to Yecheng Road and returns to destination No.1688.

## A.11. Model structure

Our model architecture consists of two main branches. The first rasterization branch, utilizes four convolutional blocks with varying scales to extract short and long-range features, which are then used to derive the scene embedding. Subsequently, the output from the rasterization branch is fed into two identical-structured decoders, each containing four sub-blocks of deconvolution layers, allowing for step-by-step upsampling to match the size of the input from the rasterization branch. The decoders generate cost volumes and prediction grid maps.

Concurrently, the vectorization branch processes parametric instance information through a PointNet subgraph, which includes three edge convolutions. The output from this branch is then passed through a downstream Transformer encoder to obtain the instance encoding.

Following the extraction of the scene embedding, features by oriented crop around the agents are obtained. These features are then processed through a sequence of maxpooling and a multi-layer perceptron (MLP). The resulting features are concatenated with the instance encoding to create the agent encoding, which is subsequently decoded by an MLP to obtain each agent's trajectory.

## A.12. Training details

The Adam optimizer is used with an initial learning rate of  $5xe^{-4}$  and a batch size of 32. The scheduler of reduce on loss plateau decay is also implemented, with a reducing factor of 0.3 and a patience factor of 2, which means that if there is no improvement after 2 epochs, the learning rate will be reduced by 0.3 times the original value. The lower bound of the learning rate is set to  $10^{-8}$  and the model parameters are randomly initialized. Experiments are conducted with 4 NVIDIA H800 GPUs with 60 epochs to complete.

Add two stage training @weijian.sun





Figure 4. Test Drive Route